Surface defect detection in low-contrast images using basis image representation

Du-Ming Tsai*
Yuan-Ze University
135, Yuan-Tung Rd., Chung-Li, Taiwan, R.O.C.
iedmtsai@saturn.yzu.edu.tw

Yan-Hsin Tseng
Yuan-Ze University
135, Yuan-Tung Rd., Chung-Li, Taiwan, R.O.C.
s939502@mail.yzu.edu.tw

Wei-Yao Chiu
Industrial Technology Research Institute
195, Sec. 4, Chung Hsing Rd., Hsinchu, Taiwan, R.O.C.
willchiu@itri.org.tw

Abstract

In this paper, we propose a machine vision approach for detecting local irregular brightness in low-contrast surface images and, especially, focus on mura (brightness non-uniformity) defects in Liquid Crystal Display (LCD) panels. A mura defect embedded in a low-contrast surface image shows no distinct intensity from its surrounding region, and even worse, the sensed image may also present uneven illumination on the surface. All these make the mura defect detection in low-contrast surface images extremely difficult.

A set of basis images derived from defect-free surface images are used to represent the general appearance of a clear surface. An image to be inspected is then constructed as a linear combination of the basis images, and the coefficients of the combination form the feature vector for discriminating mura defects from clear surfaces. In order to find minimum number of basis images for efficient and effective representation, the basis images are designed such that they are both statistically independent and spatially exclusive. An independent component analysis-based model that finds both the maximum negentropy for statistical independency and minimum spatial correlation for spatial redundancy is proposed to extract the representative basis images. Experimental results have shown that the proposed method can effectively detect various mura defects in low-contrast LCD panel images.

1. Introduction

Image analysis techniques have played an important role in manufacturing for automated visual inspection of surface defects. In automated surface inspection, defects which appear as local anomalies embedded in regular surfaces must be reliably detected. Most of the existing defect detection methods for uniform surfaces use simple thresholding or edge detection techniques [1-4]. Defects in these images can be easily detected because they commonly have distinctly measured values with respect to those of the uniform background. The inspection task in the present paper is the detection of defects in uniform surfaces that involve low-contrast intensities in images. The currently existing methods cannot be used to identify the hardly visible defects in a low-contrast image.

2. Basis image representation and defect detection

Liquid Crystal Display (LCD) panels have been important components used for a variety of electronic devices such as TV sets, PC monitors, mobile phones and digital cameras. The LCD surfaces investigated in this study present non-uniform intensities in different regions from image to image. Figure 1 demonstrates a variety of mura defects, in which (a1) is a faultless LCD surface image, and (a2)-(a5) present four mura images including white spot-, black spot-, line- and gravity-mura, respectively. Figures 1(b1)-(b5) illustrate the respective enhanced images of Figures 1(a1)-(a5). LCDs generally have the intrinsic non-uniformity due to the variance of the backlight and uneven distributions of liquid crystal material [5]. The enhanced images, therefore, result in distinctly uneven illumination, which makes the defect detection task in enhanced images even more difficult and complicated.

In this study, we organize a set of defect-free samples as a data matrix $\boldsymbol{D}$, where each row vector is a training image. It is assumed that the observed data $\boldsymbol{D}$ is a linear combination of basis images $\boldsymbol{Y}$, i. e,

$$\boldsymbol{D} = \boldsymbol{B}\boldsymbol{Y} \tag{1}$$

where $\boldsymbol{B}$ is the coefficient matrix for the linear construction. Note that the proposed model in eq. (1)

for mura defect detection is exactly of the same form as the Independent Component Analysis (ICA) model.

For a test image $\boldsymbol{d}$, it can be synthesized as a linear combination of the basis images $\boldsymbol{Y}$, i.e.,

$$\boldsymbol{d} = \boldsymbol{b} \cdot \boldsymbol{Y} = \sum_{i=1}^{N} b_i \cdot \boldsymbol{y}_i \tag{2}$$

where $\boldsymbol{b} = (b_1, b_2, ..., b_N)$ is the coefficient vector, and $\boldsymbol{y}_i$ is the i^{th} basis image, i.e., the i^{th} row vector in $\boldsymbol{Y}$, assuming there are N basis images. The coefficient vector $\boldsymbol{b}$ can be obtained by

$$\boldsymbol{b} = \boldsymbol{d} \cdot \boldsymbol{Y}^{+} \tag{3}$$

where $\boldsymbol{Y}^{+}$ is the pseudo-inverse of $\boldsymbol{Y}$, and is given by $\boldsymbol{Y}^{\mathrm{T}}(\boldsymbol{Y} \cdot \boldsymbol{Y}^{\mathrm{T}})^{-1}$.

The coefficient vector $\boldsymbol{b}$ is used as the feature vector for test image $\boldsymbol{d}$. In order to efficiently compute the coefficient vector for manufacturing implementation, the number of representative basis images should be as small as possible so that the matrix size of $\boldsymbol{Y}^{+}$ and the dimension of $\boldsymbol{b}$ can be small.

Assume that there are a total of N training images in the data matrix $\boldsymbol{D} = [\boldsymbol{d}_1, \boldsymbol{d}_2, ..., \boldsymbol{d}_N]^{\mathrm{T}}$. The coefficient vector $\boldsymbol{b}_i$ of the training image $\boldsymbol{d}_i$ is obtained from $\boldsymbol{b}_i = \boldsymbol{d}_i \cdot \boldsymbol{Y}^{+},\ i = 1, 2, ..., N$.

The mean coefficient vector $\bar{\boldsymbol{b}}$ is given by

$$\bar{\boldsymbol{b}} = \frac{1}{N} \sum_{i=1}^{N} \boldsymbol{b}_i \tag{4}$$

In the defect-detection stage, the similarity between a test image $\boldsymbol{d}_t$ with feature vector $\boldsymbol{b}_t$ and the representative defect-free image with feature vector $\bar{\boldsymbol{b}}$ can be measured by Euclidean distance:

$$\Delta b_e = \left\| \bar{\boldsymbol{b}} - \boldsymbol{b}_t \right\| \tag{5}$$

or Cosine distance:

$$\Delta b_c = 1 - \frac{\bar{\boldsymbol{b}} \cdot \boldsymbol{b}_t}{\left\| \bar{\boldsymbol{b}} \right\| \cdot \left\| \boldsymbol{b}_t \right\|} \tag{6}$$

The selected basis images from a set of defect-free training images should have maximum statistical independency and minimum spatial redundancy. Let $\boldsymbol{D} = [\boldsymbol{d}_1, \boldsymbol{d}_2, ..., \boldsymbol{d}_N]^{\mathrm{T}}$ be the data matrix of N training defect-free images and $\boldsymbol{Y}=\boldsymbol{WD}$, where $\boldsymbol{Y} = [\boldsymbol{y}_1, \boldsymbol{y}_2, ..., \boldsymbol{y}_N]^{\mathrm{T}}$ and $\boldsymbol{W} = [\boldsymbol{w}_1, \boldsymbol{w}_2, ..., \boldsymbol{w}_N]^{\mathrm{T}}$. Each 2D training image $\boldsymbol{I}_i$ of size $m \times n$, for $i = 1, 2, \cdots, N$, is converted to a vector $\boldsymbol{d}_i$ of length $L = m \cdot n$ by scanning the pixels from left to right and top to bottom. The vector image $\boldsymbol{d}_i$ is then organized as a row vector in the data matrix $\boldsymbol{D}$. To achieve the maximum statistical independency, the first objective of the proposed method evaluates the negentropy of the basis images $\boldsymbol{Y}$. That is

$$\text{Max. } J(\boldsymbol{Y}) = \sum_{i=1}^{N} E[G(\boldsymbol{y}_i)]^2 \tag{7a}$$

where $\boldsymbol{y}_i = [y_{i1}, y_{i2}, \cdots, y_{iL}]$, and

$$E[G(\boldsymbol{y}_i)] = \frac{1}{L} \sum_{k=1}^{L} \left[-\exp(-y_{ik}^2 / 2) \right],\ i = 1, 2, \cdots, N \tag{7b}$$

The objective of maximum negentropy considers only the statistical independency based on the probability distributions of gray values among the basis images. To achieve the minimum spatial redundancy, the correlation coefficient between any two basis images is used as the measure. The correlation coefficient evaluates the consistency of two signals at coincident locations. If the correlation coefficient between two signals is high, then they can be considered to be spatially duplicated. The objective of minimum spatial redundancy of basis images is given by the MinMax principle:

$$\text{Min} \max_{i \neq j} \delta(\boldsymbol{y}_i, \boldsymbol{y}_j)^2 \tag{8a}$$

$$\text{where } \delta(\boldsymbol{y}_i, \boldsymbol{y}_j) = \frac{\frac{1}{L} \sum_{k=1}^{L} (y_{ik} - \bar{y}_i) \cdot (y_{jk} - \bar{y}_j)}{\sqrt{\frac{1}{L} \sum_{k=1}^{L} (y_{ik} - \bar{y}_i)^2 \cdot \frac{1}{L} \sum_{k=1}^{L} (y_{jk} - \bar{y}_j)^2}} \tag{8b}$$

$\bar{y}_i$ and $\bar{y}_j$ are the mean values of all elements in basis images $\boldsymbol{y}_i$ and $\boldsymbol{y}_j$, respectively.

Since we would like to simultaneously maximize the statistical independency and minimize the spatial redundancy of the basis images, the two separate objectives above is merged as a dual-objective model, i.e.,

$$\text{Min} \{ \max_{i \neq j} \delta(\boldsymbol{y}_i, \boldsymbol{y}_j)^2 / \sum_i E[G(\boldsymbol{y}_i)]^2 \} \tag{9}$$

The model comprises two parts, where the objective Min $\max_{i \neq j} \delta(\boldsymbol{y}_i, \boldsymbol{y}_j)^2$ in eq. (9) tends to minimize the worst case of spatial redundancy between any two basis images, and the objective Min $1/J(\boldsymbol{Y})$ in eq. (9) tries to make the basis images as statistically independent as possible.

The dual-objective model proposed involves a non-differential function. It is therefore solved by a particle swarm optimization (PSO) algorithm [6, 7]. The model defined in eq. (9) sets up the objective to achieve for some unknown transformation matrix $\boldsymbol{W}$. The stochastic search procedure of PSO can find automatically the best matrix $\boldsymbol{W}$ to minimize the objective.

3. Experimental results

This section presents the experimental results from a number of low-contrast LCD images to evaluate the performance of the proposed method. All of the training and test images in the experiments are 256×256 pixels wide with 8-bit gray levels. The training images used to form the data matrix are randomly sampled from defect-free LCD panel surfaces.

Four defect-free and four defective low-contrast surface images of LCD panels containing white spot-, black spot-, line- and gravity-mura, as seen in Figures 1(a2)-(a5), are first used as the test samples for demonstrating the efficacy of the proposed method. Three faultless LCD panel images are used as the training images and, therefore, three basis images are obtained. The mean coefficient vector of the three resulting basis images derived from the PSO search of the proposed dual-objective model is $\bar{\boldsymbol{b}}$ = [0.0789, 0.5711, 0.0313]. It gives a Euclidean distance of 0.8165 and a cosine distance of 0.4427 to the training sample images. Tables 1 summarize, respectively, the resulting Euclidean and cosine distances for the four defective sample images from four different models. The first model is the proposed dual-objective that takes into account both statistical independency and spatial redundancy. The second model is given by $\underset{i \neq j}{Min\,Max}\, \delta(\boldsymbol{y}_i, \boldsymbol{y}_j)^2$, i.e., the basis images estimated should have minimum spatial redundancy. The third model is to maximize the negentropy $J(\boldsymbol{Y})$, i.e., the basis images should be statistically independent as possible. The basis images derived from models 2 and 3 are also based on the PSO algorithm. The fourth model is also a measure of maximum negentropy, but solved with the FastICA algorithm [8]. The demonstrated results in Tables 1 and 2 show that only the proposed method can effectively detect defective images with either the Euclidean or cosine distance. The measured distances for the defective images are distinctly different from those for the defect-free images by using the proposed dual-objective model.

In order to further verify the detection performance of the proposed method, a total of 48 LCD sample images are evaluated, of which 20 are defect-free and 28 are defective. The measured results are presented as box-plots, and are shown in Figures 2 and 3. The box plot shows the minimum, maximum, lower and upper quartiles, and the median of the distance distribution of the test samples for each of the four models. Figures 2(a) and 3(a) show that the proposed dual-objective model can well distinguish the faultless and defective LCD images with both Euclidean and cosine distances. The distance distributions of the faultless and defective test samples are overlapped for the remaining three models.

The proposed method was implemented on a Pentium 4, 3.2GHz personal computer. The computation time of the proposed algorithm with four basis images in the defect-detection stage is only 0.0081 seconds for an image of size 256×256 pixels. Even with five basis images, the total inspection time is only 0.4752 seconds for a 17” LCD panel, which usually requires 120 seconds for human inspection. It indicates that the proposed method is practical for on-line, real-time implementation in LCD manufacturing.

4. Conclusions

The proposed method aims at the inspection of LCD panel surfaces that contain low-contrast mura defects of various sizes and shapes. Experimental results have shown that the proposed method can effectively detect both small-sized, low-contrast defects such as spot-mura and line-mura, and large-sized defects without clear edges such as the hardly-detectable gravity-mura. Besides mura defect detection in LCD panel surfaces, it is believed that the proposed method can be applied in general for the inspection of surface defects in any low-contrast images.

References

[1] J. Wilder, Finding and evaluating defects in glass, In: Machine Vision for Inspection and Measurement, H. Freeman (Ed.), Academic Press, New York, 1989, p. 237.

[2] J. Olsson, S. Gruber, Web process inspection using neural classification of scattering light, Proceedings of the IEEE International Conference on Industrial Electronics, Control, Instrumentation and Automation (IECON’92), 1992, pp. 1443-1448.

[3] C. Fernandez, D. Platero, P. Campoy, R. Aracil, Vision system for on-line surface inspection in aluminum casting process, Proceedings of the IEEE International Conference on Industrial Electronics, Control, Instrumentation and Automation (IECON’93), 1993, pp. 1854-1859.

[4] D. Brzakovic, N. Vujovic, Designing defect classification system: a case study, Pattern Recognition 29 (1996) 1401-1419.

[5] J. Y. Lee, S. I. Yoo, Automatic detection of region-Mura defect in TFT-LCD, IEICE Trans. Inf. and Syst. E87-D (2004) 2371-2378.

[6] J. Kennedy, R. Eberhart, Particle swarm optimization, Proceedings of the IEEE International Conference on Neural Networks, Perth, Australia, 1995, pp. 1942-1948.

[7] M. Clerc, J. Kennedy, The particle swarm-explosion, stability and convergence in a multidimensional complex space, IEEE Trans. Evol. Comput. 6 (2002) 58-73.

[8] J. Hurri, H. Gävert, J. Särelä, A. Hyvärinen, FastICA Package, Online Available: http://www.cis.hut.fi/projects/ica/fastica/.

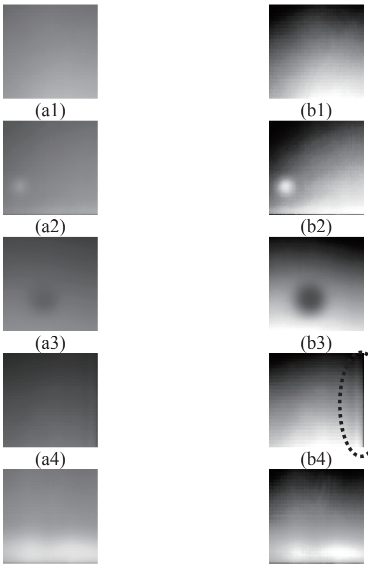

Figure 1. LCD sample images: (a1) defect-free image; (a2) white spot-mura; (a3) black spot-mura; (a4) line-mura; (a5) gravity-mura; (b1)-(b5) enhanced images of (a1)-(a5), respectively.

Table 1. Resulting Euclidean and cosine distances of demonstrative defective images (white-spot, gravity-mura, line-mura and black-spot from left to right) from four comparative models.

Defective LCD Images					
Enhanced images		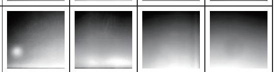			
Euclidean distances	Min $\frac{Max(\delta(\boldsymbol{y}_i,\boldsymbol{y}_j)^2)}{(E[G(\boldsymbol{Y})])^2}$	1.0591	1.8487	1.8164	2.2632
	Min Max$(\delta(\boldsymbol{y}_i,\boldsymbol{y}_j)^2)$	7.7938	16.8250	6.8048	7.8962
	$Max(E[G(\boldsymbol{Y})])^2$	3.4515	4.7356	4.7278	2.6301
	FastICA	7.1271	9.8623	9.7727	6.0115
Cosine distances	Min $\frac{Max(\delta(\boldsymbol{y}_i,\boldsymbol{y}_j)^2)}{(E[G(\boldsymbol{Y})])^2}$	0.5671	0.6367	0.6407	0.7612
	Min Max$(\delta(\boldsymbol{y}_i,\boldsymbol{y}_j)^2)$	0.0509	1.8832	1.8861	0.0544
	$Max(E[G(\boldsymbol{Y})])^2$	0.0570	0.0722	0.0780	0.0305
	FastICA	0.0595	0.0605	0.0607	0.0455

Table 2. Resulting Euclidean and cosine distances of demonstrative defect-free images from four comparative models.

Defect-free LCD Images					
Enhanced images		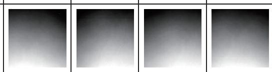			
Euclidean distances	Min $\frac{Max(\delta(\boldsymbol{y}_i,\boldsymbol{y}_j)^2)}{(E[G(\boldsymbol{Y})])^2}$	0.8165	0.3566	0.7691	0.8068
	Min Max$(\delta(\boldsymbol{y}_i,\boldsymbol{y}_j)^2)$	7.7183	1.4760	4.9428	8.7147
	$Max(E[G(\boldsymbol{Y})])^2$	1.3548	1.8340	3.1420	1.3495
	FastICA	2.7097	3.6146	6.3717	2.7046
Cosine distances	Min $\frac{Max(\delta(\boldsymbol{y}_i,\boldsymbol{y}_j)^2)}{(E[G(\boldsymbol{Y})])^2}$	0.3935	0.2882	0.1998	0.3935
	Min Max$(\delta(\boldsymbol{y}_i,\boldsymbol{y}_j)^2)$	0.9317	0.0379	1.5301	0.0244
	$Max(E[G(\boldsymbol{Y})])^2$	0.4227	0.2042	0.4142	0.4200
	FastICA	0.0379	0.0663	1.5527	0.0306

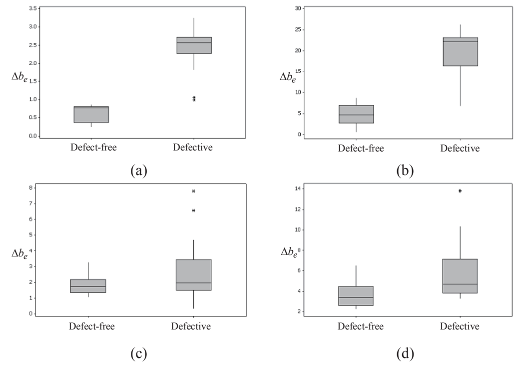

Figure 2. Box-plots of Euclidean distances from four different models: (a) proposed dual-objective; (b) $\text{Min Max}\delta(\boldsymbol{y}_i, \boldsymbol{y}_j)^2$; (c) Max $J(\boldsymbol{Y})$; (d) *FastICA*.

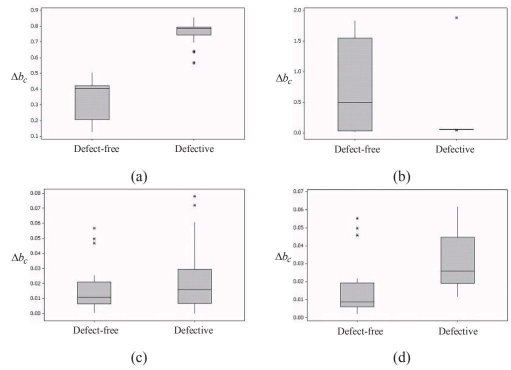

Figure 3. Box-plots of cosine distances from four different models: (a) proposed dual-objective; (b) $\text{Min Max}\delta(\boldsymbol{y}_i, \boldsymbol{y}_j)^2$; (c) Max $J(\boldsymbol{Y})$; (d) *FastICA*.